Layered Double Hydroxide Modified Bone Cement Promoting Osseointegration *via* Multiple Osteogenic Signal Pathways

Yingjie Wang[#a], Songpo Shen[#b, a], Tingting Hu[c], Gareth R. Williams[d], Yanyan Bian[a], Bin Feng[a], Ruizheng Liang[*c], Xisheng Weng[*a]

[a] *Department of Orthopedic Surgery, Peking Union Medical College Hospital, Peking Union Medical College & Chinese Academy of Medical Sciences, Beijing 100730, China.*

[b] *Department of Orthopedic Surgery, Beijing Tongren Hospital, Capital Medical University, Beijing 100730, China*

[c] *State Key Laboratory of Chemical Resource Engineering, Beijing Advanced Innovation Center for Soft Matter Science and Engineering, Beijing University of Chemical Technology, Beijing 100029, China.*

[d] *UCL School of Pharmacy, University College London, 29-39 Brunswick Square, London WC1N 1AX, UK.*

[#] Yingjie Wang and Songpo Shen contributed equally to this work.

***** Corresponding authors: liangrz@mail.buct.edu.cn (R. L.); xshweng@pumch.cams.cn (X. W.).

ABSTRACT

Polymethyl methacrylate (PMMA) bone cement has been widely used in orthopedic surgeries including total hip/knee replacement, vertebral compression fracture treatment, and bone defect filling. However, aseptic loosening of the interface between PMMA bone cement and bone often leads to failure. Hence, the development of modified PMMA that facilitates the growth of bone into the modified PMMA bone cement is key to reduce the incidence of aseptic loosening. In this study, MgAl-layered double hydroxides (LDH) microsheets modified PMMA (PMMA&LDH) bone cement with superior osseointegration performance has been synthesized. The maximum polymerization reaction temperature of PMMA&LDH decreased by 7.0 and 11.8 ℃ respectively compared with that of PMMA and PMMA&COL-I (mineralized collagen I modified PMMA). The mechanical performance of PMMA&LDH decreased slightly in comparison with PMMA, which is beneficial to alleviate stress-shielding osteolysis, and indirectly promote osseointegration. The superior osteogenic ability of PMMA&LDH has been demonstrated *in vivo*, which boosts bone growth by 2.17- and 18.34- fold increment compared to the PMMA&COL-I and PMMA groups at 2 months postoperatively. Moreover, transcriptome sequencing revealed four key osteogenic pathways: p38 MAPK, ERK/MAPK, FGF, and TGF-β, which were further confirmed by IPA, qPCR, and western blot assays. Hence, LDH modified PMMA bone cement is a promising biomaterial to enhance bone growth with potential applicaions in relevant orthopedic surgeries.

KEYWORDS: polymethyl methacrylate, layered double hydroxides, mechanical properties, osteogenesis, signal pathways

Bone cement has been widely used in total hip/knee replacement, minimally invasive treatment of vertebral compression fractures, bone tumors, bone defect, and many other orthopedic procedures.[1-4] At present, the mainstream bone cement used in clinic worldwide is polymethylmethacrylate (PMMA). In 1946, PMMA bone cement was applied to orthopedics by Robert Judet of France.[5] Since then, it has been applied in clinical use and its safety and clinical effects have been widely recognized. However, the PMMA bone cement has a few shortcomings: (i) the biological inertness, undegradability,[6] and potential cytotoxic properties[7] hinder the bone formation into PMMA; (ii) the high polymerization temperature will cause the death of surrounding osteoblast-related cells and the subsequent formation of a fibrotic film will hinder the osseointegration of PMMA bone cement and bone;[8] (iii) the excessive elastic modulus can lead to stress-shielding osteolysis.[9,10] Thus, PMMA can't form biological osseointegration at the implantation site due to the above shortcomings, and leads to aseptic loosening of bone cement, which has become the dominant factor for more than 75% of failures of total hip/knee replacement.[11-13] It has proved that aseptic loosening mainly occurs at the interface of bone cement and bone.[10,14] Therefore, how to regulate and modify PMMA bone cement with improved osteogenic activity, decreased polymerization temperature, and reduced elastic modulus so as to promote osseointegration has been a big challenge.

To date, many materials have been added to improve the mechanical properties, biocompatibility, and osteogenesis of PMMA bone cement, such as hydroxyapatite or strontium-doped hydroxyapatite,[15-17] biodegradable chitosan and sodium hyaluronate.[18-20] However, the addition of hydroxyapatite and biodegradable component can largely decrease the compressive strength of bone cement.[20-22] Moreover, the addition of above materials brings no efficient

osteogenesis performance. Layered double hydroxides (LDHs) are a class of two-dimensional nanomaterials consisting of edge-sharing MO_6 octahedral host layers and negatively-charged interlayer anions.[23-27] Due to the versatile structure and good biocompatibility, LDHs have drawn extensive attention in biomedical fields such as bone repair, cancer therapy, and drug delivery.[27-30] LDHs are excellent thermal insulation materials too and the assembly of LDHs with polymers can obviously improve their mechanical properies.[31-35] Therefore, if magnesium-based LDH microsheets were utilized to modify PMMA, the following advantages can be expected to overcome the current limitations of PMMA bone cement: (i) the superior thermal insulation properties of LDHs could probably inhibit the thermal diffusion in the process of polymerization reaction of MMA, and contribute to the protection of surrounding osteoblast-related cells; (ii) the magnesium ions released from LDHs would promote osteogenesis; (iii) the large size of LDHs microsheets can produce a certain number of pores on PMMA surface, which is beneficial to the osteointegration between the bone cement and bone.

Whether LDH modified PMMA can advantageously affect the mechanical and physical properties as well as osteogenic capability is still unknown. Therefore, the aim of our study is to investigate relevant mechanical and physical properties as well as *in vitro* and *in vivo* biological performance of LDH modified PMMA. It is hypothesized that LDH modified PMMA can improve the mechanical and physical properties and biocompatibility of PMMA, and as a result it will endow PMMA with osteogenic capacity *in vivo* and *in vitro*. Therefore, we measured the peak heat of polymerization and setting time of LDH modified PMMA, and detected its mechanical properties by a universal material testing machine. Moreover, the biocompatibility of LDH modified PMMA was measured by cell count kit-8 and flow cytometry assays, while its osteogenic capability was reflected

by alkaline phosphatase and alizarin red S staining assays. The mechanism of osteogenic capability was further revealed by transcriptome sequencing and subsequent confirmatory experiments including western blot and quantitative real-time polymerase chain reaction. In addition, the osteogenic capability of LDH modified PMMA was further investigated *in vivo* based on a rabbit calvarial defect model.

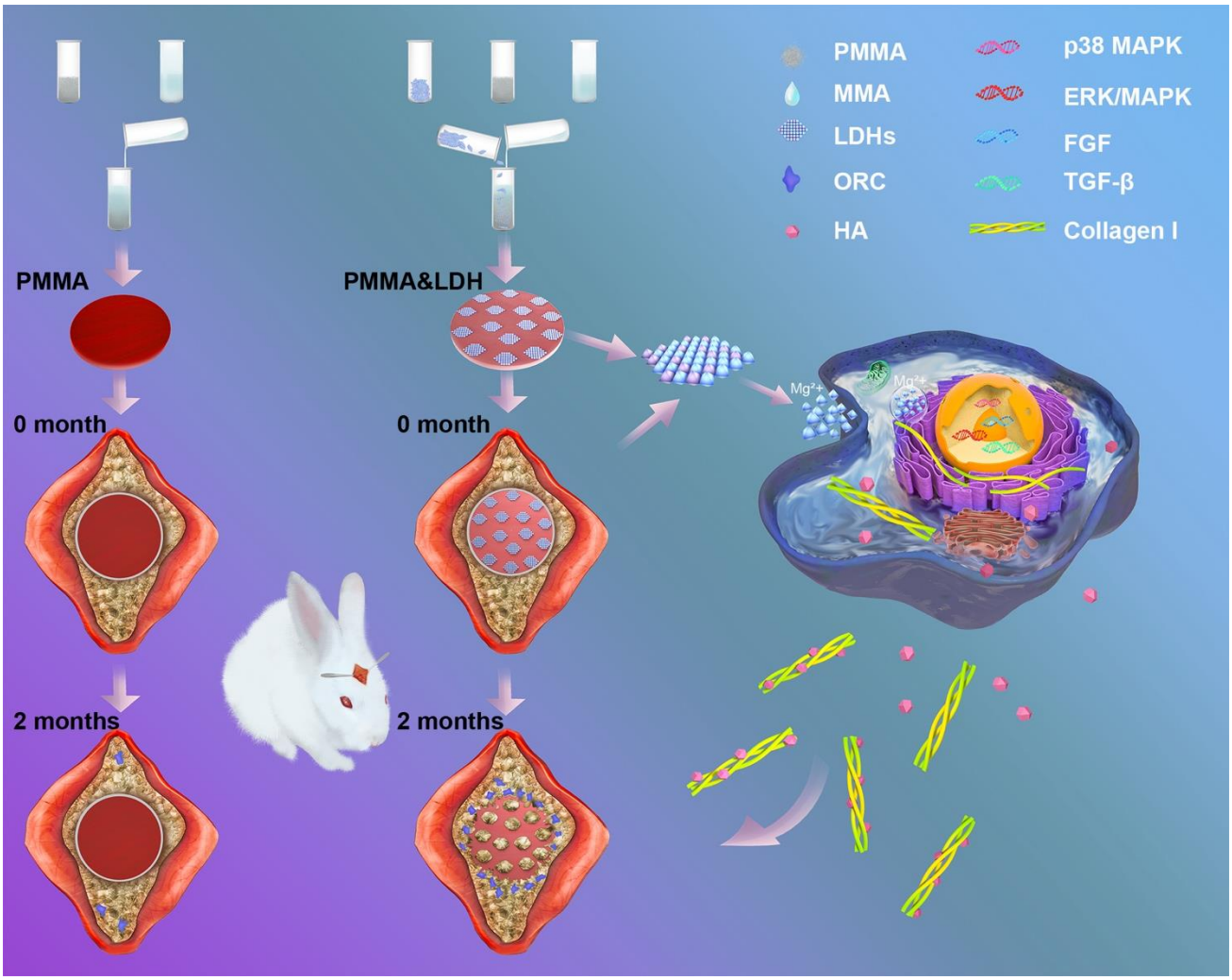

Scheme 1. A schematic illustration for the preparation of MgAl-LDH microsheets modified PMMA (PMMA&LDH) and PMMA bone cement, and the bone formation mechanism in the presence of PMMA&LDH.

RESULTS AND DISCUSSION

Structure Characterization of LDHs and COL-I and/or LDHs Modified PMMA. MgAl-LDHs microsheets with the Mg/Al ratio of 2:1 were synthesized *via* a mild method according to previous studies.[29] XRD analysis was adopted to monitor the crystal structure of MgAl-LDHs. As shown in Figure 1a, the characteristic reflection of LDHs (003), (006), (009), and (110) phase are observed, indicating the formation of multilayer structure in MgAl-LDHs. SEM image reveals that MgAl-LDHs consist of hexagonal nanosheets with a diameter distribution of *circa* 6 ± 2 μm (Figure 1b) and microsize porous structures on the surface of PMMA&LDH and PMMA&COL-I&LDH caused by the degradation of LDH are beneficial for osteogenesis.[36,37] Figure 1c-f display the morphology of PMMA, PMMA&COL-I, PMMA&LDH, and PMMA&COL-I&LDH after COL-I and/or LDH modification. The surface roughness of PMMA, PMMA&COL-I, PMMA&LDH, and PMMA&COL-I &LDH is 0.38 ± 0.02 μm, 0.82 ± 0.02 μm, 1.57 ± 0.09 μm and 1.93 ± 0.07 μm, respectively (Figure S1). Subsequently, X-ray energy dispersive spectrometer (EDS) mappings were used to determine the composition of PMMA, PMMA&COL-I, PMMA&LDH, and PMMA&COL-I&LDH. As can be seen in Figure S2, the major elements of C and O exhibit homogeneous distribution in PMMA. In addition to C and O elements, the as-prepared PMMA&COL-I also contain Ca, N, and P elements derived from COL-I. In Figure 1g-h, C, O, Mg, and Al elements are found in PMMA&LDH while C, O, Ca, N, P, Mg, and Al elements are detected in PMMA&COL-I&LDH, confirming the successful mixing of PMMA, MgAl-LDHs and/or COL-I.

Subsequently, the maximum temperature and setting time in the polymerization reaction of MMA after adding COL-I and/or LDH was investigated. The temperature change curve of the polymerization reaction of PMMA, PMMA&COL-I, PMMA&LDH, and PMMA&COL-I&LDH are shown in Figure 1i and Figure S3. The maximum temperature of PMMA is 95.2 ℃, and the addition

of COL-I (PMMA&COL-I) and COL-I&LDH (PMMA&COL-I&LDH) increased the maximum temperature by 4.8 ℃ and 3.1 ℃, respectively. However, compared with PMMA, the maximum temperature of LDH modified PMMA (PMMA&LDH) decreased by 7.0 ℃. Hence, the addition of LDH could decrease the maximum temperature of MMA polymerization reaction due to the thermal insulation of LDH, which would probably reduce the thermal damage of osteogenic related cells around LDH modified PMMA.[38,39] Moreover, the setting time of PMMA, PMMA&COL-I, PMMA&LDH, and PMMA&COL-I&LDH detected by Vicat needle is 9.0 min, 8.8 min, 9.8 min, and 9.7 min, respectively (Figure 1j). The addition of LDH and/or COL-I didn't significantly change the operable property (setting time) of PMMA, although there are statistical differences in setting time between PMMA, PMMA&COL-I, PMMA&LDH, and PMMA&COL-I&LDH.

Hydroxyapatite (HA) and chitosan were added to PMMA to prepare bioactive bone cements. However, the mechanical properties of PMMA bone cement after modification fail to meet the requirements of ISO 5833.[21] *N*-methyl pyrrolidone monomer or linoleic acid were employed to partially replace methyl methacrylate (MMA) monomer, but resulted in decreased mechanical properties of modified PMMA bone cement.[40,41] For comparison, the mechanical properties of PMMA and LDH and/or COL-I modified PMMA were tested (Figure S4). The compressive modulus of PMMA, PMMA&COL-I, PMMA&LDH, and PMMA&COL-I&LDH shows no significant statistical difference (Figure 1k). The addition of LDH and/or COL-I reduces the bending modulus of PMMA, but the bending modulus is still higher than the minimum standard of 1.8 GPa in ISO 5833 (indicated by the pink line in Figure 1l). Moreover, the compressive strength of PMMA&COL-I,

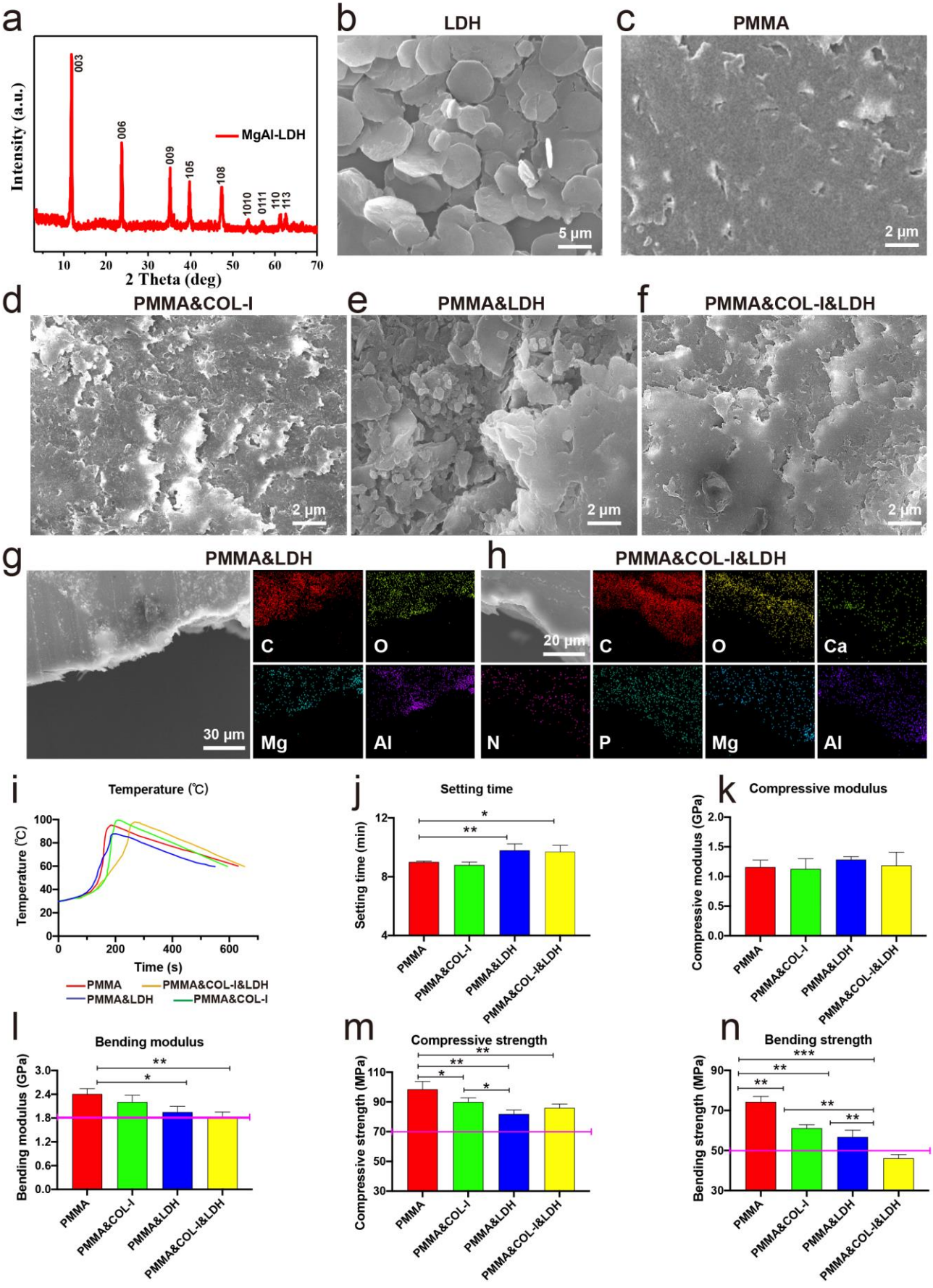

Figure 1. Structure characterization, chemical and physical properties of LDHs and LDH and/or

COL-I modified PMMA. (a) XRD patterns and (b) SEM image of MgAl-LDHs. (c-f) SEM images of PMMA, PMMA&COL-I, PMMA&LDH, and PMMA&COL-I&LDH. (g, h) EDS mappings of PMMA&LDH and PMMA&COL-I&LDH. (i) Temperature changes in the process of polymerization reaction. The setting time detected by the Vicat needle (j). Mecahnical properties including compressive modulus (k), bending modulus (l), compressive strength (m), and bending strength (n). *p < 0.05, **p < 0.01, ***p < 0.001 (N =3, one–way ANOVA followed by the Student–Newman–Keuls post hoc test).

PMMA&LDH, and PMMA&COL-I&LDH is lower than that of PMMA by 8.68%, 16.87%, and 12.70% respectively, which are obviously greater than the lower limit of 70 MPa according to IOS 5833 (indicated by the pink line in the Figure 1m). Furthermore, the addition of COL-I or LDH reduces the bending strength of PMMA by 17.72% and 23.66%, and the bending strength of PMMA&COL-I&LDH fails to meet the criteria of IOS 5833 (Figure 1n). Therefore, the addition of COL-I or LDH may alleviate stress-shielding osteolysis and indirectly promote osseointegration.[9,42]

The Evaluation of Biocompatibility *in vivo* and *in vitro.* Based on the superior physical-chemical properties, biocompatibility of PMMA, PMMA&COL-I, PMMA&LDH, and PMMA&COL-I&LDH groups *in vitro* was further studied using human bone marrow-derived mesenchymal stem cells (hBMSCs). After cultured for 1, 3, 5, and 7 days, the cell viability treated with PMMA, PMMA&COL-I, PMMA&LDH, and PMMA&COL-I&LDH by indirect (Figure 2a) and direct contact (Figure 2b) was determined by CCK 8 assay. As depicted in Figure 2a-b, the optical density (OD) values of the four groups increase gradually with incubation time and exhibit similar tendency to the blank control group. It is worth noting that the cell viability of PMMA&COL-I, PMMA&LDH, and PMMA&COL-I&LDH is 1.55-, 1.43-, and 1.48- times higher than that of PMMA respectively (Figure 2a). To further confirm the results of CCK 8, flow

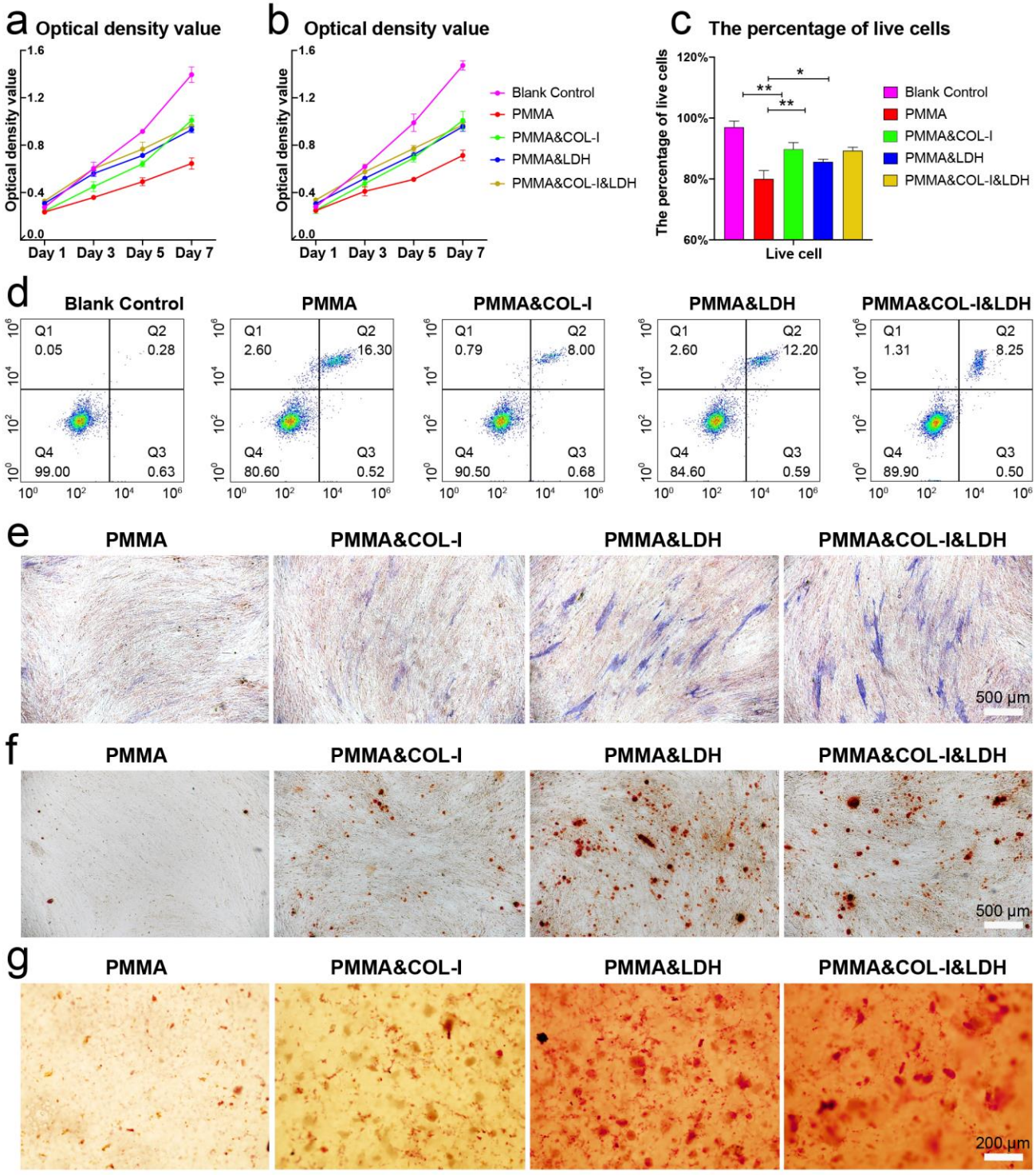

Figure 2. Cytocompatibility and osteogenic differentiation of PMMA, LDH and/or COL-I modified PMMA *in vitro*. Cytocompatibility of indirect contact (a) and direct contact (b) reflected by CCK 8 assay on Day 1, 3, 5, and 7. (c-d) Live cells determined by flow cytometry assay using annexin-V/propidium iodide (AV/PI) on Day 3. Results are presented as the percentage of live cells (Q4), early apoptosis cell (Q3), late apoptosis cell (Q2), and necrosis cell (Q1). (e) Alkaline phosphatase staining: blue stained areas representing alkaline phosphatase. Scale bar: 500 μm. (f-g)

Alizarin red S staining: calcium nodules are stained red in extracellular matrix mineralization. Scale bar: 500 μm (f), 200 μm (g). *p < 0.05, **p < 0.01 (N =3, one–way ANOVA followed by the Student–Newman–Keuls post hoc test).

cytometry was performed and the percentage of live cells in blank control, PMMA, PMMA&COL-I, PMMA&LDH, and PMMA&COL-I&LDH groups is determined to be 99.0%, 80.6%, 90.5%, 84.6%, and 89.9%, respectively (Figure 2c-d). Both the results of CCK 8 and flow cytometry assays demonstrate that the addition of COL-I and/or LDH improve the cytocompatibility of PMMA. Moreover, the biocompatibility of PMMA, PMMA&COL-I, PMMA&LDH, and PMMA&COL-I&LDH groups *in vivo* was further evaluated. The most commonly used tissues (heart, liver, spleen, kidney, and spinal cord) to demonstrate the systemic toxicity of implants[43-46] were harvested immediately, 1 month, and 2 months after surgery, and then soaked in neutral formalin for hematoxylin-eosin staining to reveal the changes of histological structure. No difference is found in the myocardium (heart), hepatic lobule (liver), splenic cord and splenic sinus (spleen), glomerulus and kidney tubules (kidney), and H-shaped gray matter zone (spinal cord) in four groups (Figure S5-9), demonstrating satisfactory *in vivo* biocompatibility of COL-I and/or LDH modified PMMA.

Osteogenic Differentiation of hBMSCs *in vitro.* The osteogenic differentiation of hBMSCs induced by COL-I and/or LDH modified PMMA was further investigated after the evaluation of biocompatibility *in vivo* and *in vitro*. Initially, the osteogenic differentiation ability was evaluated by alkaline phosphatase (ALP) and alizarin red S staining assays on Day 14.[47,48] As shown in Figure 2e, the ALP positive cells in PMMA&LDH and PMMA&COL-I&LDH groups are significantly larger than those in PMMA and PMMA&COL-I groups. Moreover, the red-staining areas (calcium nodules stained by alizarin red S) in the extracellular matrix indirectly treated with PMMA&LDH and

PMMA&COL-I&LDH are more evident than those in PMMA and PMMA&COL-I groups (Figure 2f). Furthermore, the calcium nodules in the extracellular matrix of hBMSCs cultured directly on the surface of PMMA&LDH and PMMA&COL-I&LDH are also more apparent than those in PMMA and PMMA&COL-I groups (Figure 2g). All the results above demonstrate the good osteogenic ability of LDH modified PMMA. The magnesium ions concentrations released from PMMA&LDH and PMMA&COL-I&LDH bone cements are about 1.60 and 1.31 μmol/mL, respectively (Figure S10). The moderate magnesium ions concentrations produced by PMMA&LDH and PMMA&COL-I&LDH bone cements are beneficial to promote the osteogenic differentiation of human BMSCs.[49,50]

Transcriptome sequencing was further performed to reveal the mechanism of osteogenic differentiation induced by PMMA&LDH in comparison with PMMA,[51-53] and the process of database construction and bioinformatics analysis of transcriptome sequencing were shown in Figure S11. The total number of differentially expressed genes (P value<0.05 & $|\log_2$ Fold Change|>1) is 739, which includes 367 upregulated genes and 372 downregulated genes (Figure 3a). The above differentially expressed genes were analyzed by Gene Ontology (GO) enrichment, and most of them are involved in osteogenesis and angiogenesis, including extracellular matrix organization, cell adhesion, collagen catabolic process, collagen fiber organization, blood vessel development, cellular region, extracellular matrix, extracellular matrix structural constituent, nuclear receptor activity, and E-box binding (Figure 3b). Due to the significant differences of osteogenesis and angiogenesis revealed by GO, Kyoto Encyclopedia of Genes and Genomes (KEGG) analysis was performed to reveal the key osteogenic signal pathways. Among the top 20 signal pathways, four are related to osteogenesis (the words in red font, Figure 3c). Because GO and KEGG analyses (Figure 3b-c) are

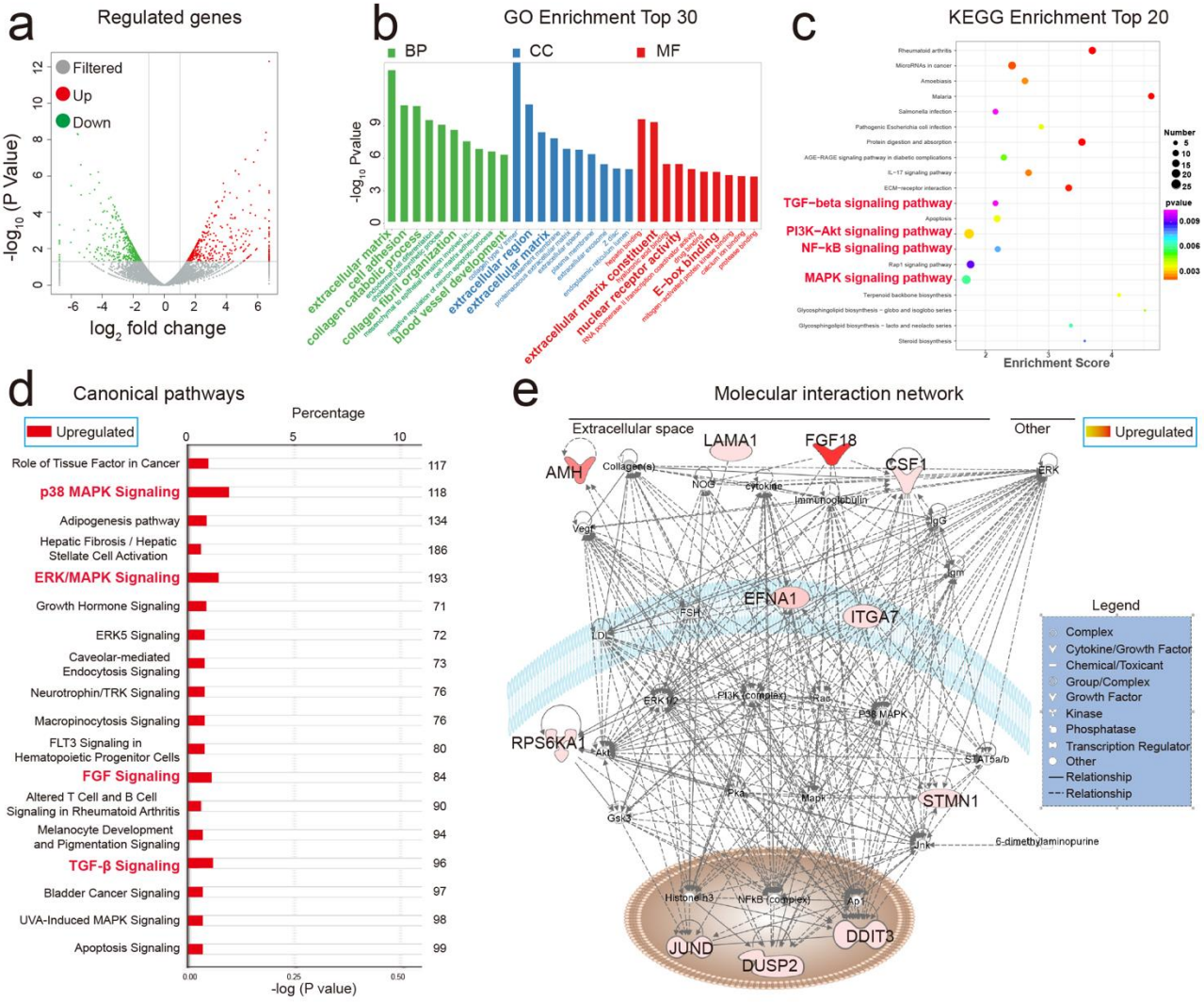

Figure 3. Results of transcriptome sequencing and Ingenuity Pathway Analysis. (a) Volcano plot visually showing the number of upregulated (red dots) and downregulated genes (green dots), Cutoff: P value<0.05 & $|\log_2 FC|>1$. (b) GO analysis indicating the biological functions of differentially expressed genes, including biological process (BP), cellular component (CC), and molecular function (MF). (c) KEGG analysis demonstrating the top 20 signal pathways enriched by differentially expressed genes. (d) Top 18 canonical pathways generated by Ingenuity Pathway Analysis software. (e) Molecular interaction network and subcellular localization of differentially expressed genes involved in osteogenesis-related signaling pathways generated by Ingenuity Pathway Analysis software.

predictable based on specific algorithms, Ingenuity Pathway Analysis (IPA®, v01-04, QIANGEN

Redwood City, CA, USA) software was utilized to reveal the true experimentally verified signal pathways and create the molecular interaction network (Figure 3d-e). Figure 3d shows that PMMA&LDH activated the p38 MAPK,[54] extracellular signal-regulated kinases (ERK)/MAPK,[55,56] FGF,[57] and TGF-β[58] signaling, all of which promote the osteogenic differentiation of hBMSCs. Additionally, Figure 3e vividly demonstrate the molecular interaction network and subcellular localization of differentially expressed genes involved in osteogenesis-related signal pathways. After a comprehensive analysis of the results of transcriptome sequencing and IPA, p38 MAPK, ERK/MAPK, FGF, and TGF-β signal pathways were selected to show the complete signal pathways, and the gene regulated by LDHs in the selected pathways are marked in red or pink[59-64] (Figure S12-15). The overlay of selected signal pathways and interaction network are shown in Figure S16 respectively.

The downstream effector molecules of p38 MAPK signaling pathway are P-p38 and p38. The increased ratio of P-p38 to p38 indicates that the p38 MAPK signaling pathway is activated.[65,66] Moreover, p38 MAPK, ERK/MAPK, FGF18, and TGF-β signal pathways were further demonstrated to enhance the osteogenic process through runt-related transcription factor 2 (*Runx2*) and alkaline phosphatase (*Alp*).[67-69] Therefore, the ratio of P-p38 to p38 as well as the transcription and translation levels of *Runx2* and *Alp* were further verified by quantitative real-time polymerase chain reaction (qPCR, Figure 4a and Table S1) and western bolt (WB) assays (Figure 4b-f), respectively. QPCR and WB assays were performed on Day 7. As shown in Figure 4a, the transcriptional level of *Runx2* for hBMSCs treated with PMMA&COL-I, PMMA&LDH and PMMA&COL-I&LDH is 1.16-, 2.01- and 2.06-times higher that those treated with PMMA respectively. Moreover, the transcriptional level of *Alp* for hBMSCs treated with PMMA&COL-I, PMMA&LDH and PMMA&COL-I&LDH is

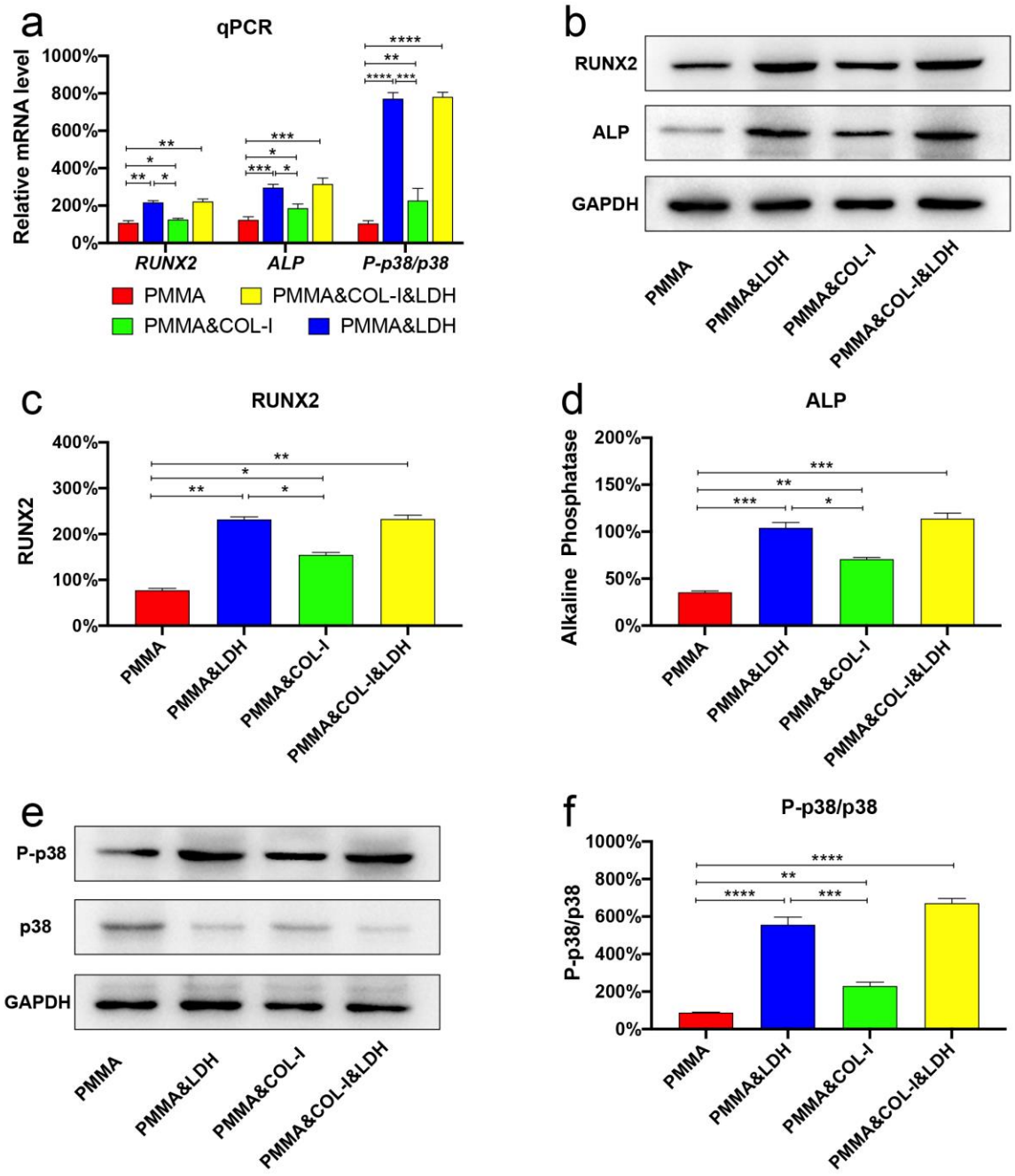

Figure 4. QPCR and WB tests were performed to verify the results of transcriptome sequencing and IPA. (a) Relative gene transcription levels of hBMSCs for osteogenic markers (*Runx2*, *Alp*, *p38,* and *P-p38*) on Day 7. Relative gene expression levels of *Runx2* (b, c) and *Alp* (b, d) were analyzed using western blot and Image J 1.52q 1.52v software. Expressions of *p38* and *P-p38* were analyzed using western blot and Image J 1.52q 1.52v software (e, f). The protein level of the blank control group was set to 1 (10^0). *p < 0.05, **p < 0.01, ***p < 0.001, ****p < 0.0001 (N =3, one–way ANOVA followed by the Student–Newman–Keuls post hoc test).

1.51-, 2.40- and 2.55-times higher than that of PMMA group. In addition, the ratio of P-p38 to p-38 in PMMA&COL-I, PMMA&LDH, and PMMA&COL-I&LDH groups is 2.17-, 7.37-, and 7.46-times higher than that of PMMA group. Besides transcription level, translational level was also detected by WB assays. The translational level of *Runx2* for hBMSCs in PMMA&COL-I, PMMA&LDH and PMMA&COL-I&LDH groups is 1.99-, 3.00- and 3.01-times higher than that of PMMA group respectively (Figure 4b-c). The translational level of *Alp* for hBMSCs in PMMA&COL-I, PMMA&LDH and PMMA&COL-I&LDH groups is 2.01-, 2.95- and 3.23-times higher than that in PMMA group, respectively (Figure 4b, 4d). The above results demonstrate that LDH can significantly promote the expression of osteigenic genes by activating p38MAPK, ERK/MAPK, FGF18, and TGF-β signal pathways. Finally, the ratio of P-p38 to p-38 in PMMA&COL-I, PMMA&LDH, and PMMA&COL-I&LDH groups is 2.62-, 6.34-, and 7.66-times higher than that in PMMA group (Figure 4e-f), indicating the activation of p38 MAPK signal pathway by LDHs. Overall, all the results of *Runx2*, *Alp, p38, and P-p38* demonstrate the superior osteogenic differentiation performance of LDH and COL-I&LDH modified PMMA.

Bone Formation into PMMA and Modified PMMA *in vivo.* Encouraged by the superior biocompatibility and osteogenic differentiation *in vitro*, the osteogenesis effect *in vivo* was further investigated using New Zealand white rabbits. The animal model of bone defect in skull was established, and then the PMMA and modified PMMA (implants) were implanted into corresponding positions (Figure S17). Newly formed bone was assessed by micro computed tomography (micro-CT), sequential fluorescent labeling assay, and acid fuchsin staining at Month 0, 1, and 2, postoperatively. Immediately postoperative images clearly demonstrate that the bone defects are

filled up with corresponding implants with obvious interface between the bone and implant (Figure 5a). According to micro-CT images at Month 1 and 2, the osseointegration between the bone and implants in group PMMA&LDH and PMMA&COL-I&LDH is significantly superior to that in group PMMA and PMMA&COL-I, and the osseointegration increases with time both on sagittal and coronal cross-sectional views (Figure 5a-b). For the quantitative analysis of newly formed bone volume, 3D construction and quantitative analysis of bone volume were performed. As shown in Figure 5c-d, the volume of bone growing into PMMA&LDH and PMMA&COL-I&LDH increases 18.34- and 17.29-times when compared with the PMMA group 2 months postoperatively. Moreover, it is worth noting that the bone volume growing into PMMA&LDH and PMMA&COL-I&LDH is 2.17- and 2.05-times larger than that into PMMA&COL-I. Two reasons account for the better ability of PMMA&LDH in promoting bone formation than PMMA&COL-I and PMMA&COL-I&LDH. For PMMA&COL-I and PMMA&LDH, the magnesium ions released from LDHs promote osteogenesis better than COL-I. For PMMA&LDH and PMMA&COL-I&LDH, the presence of COL-I occupied partial surface of PMMA&COL-I&LDH and thus the number of LDH particles exposed on the surface sites would be decreased compared with PMMA&LDH, and therefore weakened the bone formation induced by LDH microsheets. The above results of micro-CT manifest the obvious bone formation of LDH modified PMMA and COL-I&LDH modified PMMA bone cements *in vivo*. Moreover, fluorescent labeling (Figure 5e-f) and acid fuchsin stain assays (Figure 5g-h) were utilized to analyze the degree of bone growing into the implants, and the results is similar to that of micro-CT. All the results indicate that LDH and COL-I&LDH modified PMMA can be used as effective biomaterials to enhance the osseointegration of interface between the bone and bone cement, and possibly prevent the occurrence of aseptic loosening.[9]

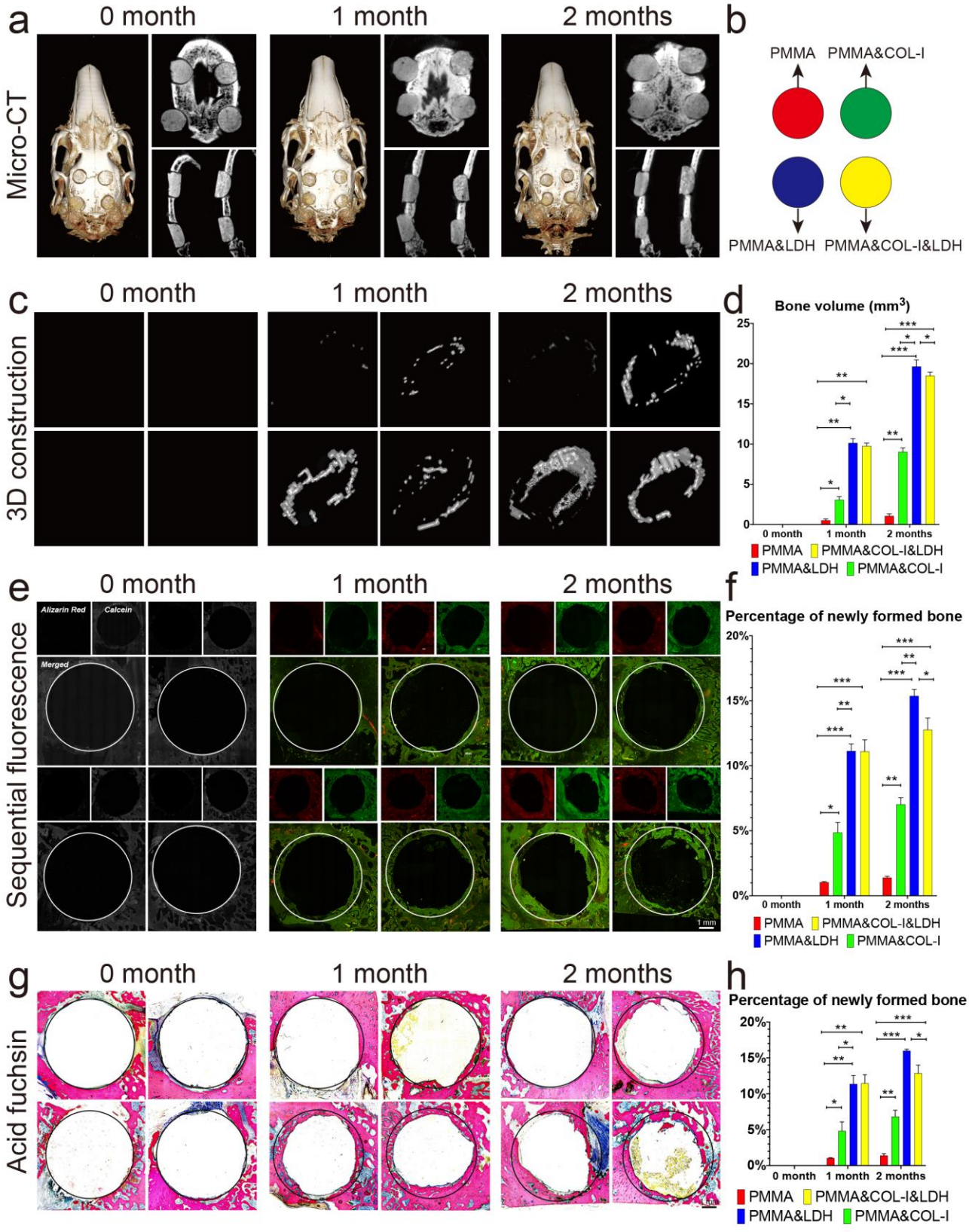

Figure 5. Bone formation *in vivo* detected by micro-CT, laser scanning confocal microscopy scanning, and acid fuchsin stain. (a) Representative cross-sectional views of 3D construction, sagittal

and coronal cross-section at 0, 1, and 2 months postoperatively. (b) PMMA, PMMA&COL-I, PMMA&LDH, and PMMA&COL-I&LDH were implanted into corresponding positions. 3D construction of newly formed bone and quantitative analysis (c, d). Representative views and quantitative analysis of sequential fluorescent labeling assay (e, f) and acid fuchsin stain (g, h). The diameter of the circle: 6 mm (e, g). Scale bar: 1 mm (e, g). *$p < 0.05$, **$p < 0.01$, ***$p < 0.001$ (N =3, one–way ANOVA followed by the Student–Newman–Keuls post hoc test).

CONCLUSIONS

During the past decades, researchers have been devoted to endowing bioinert PMMA bone cement with bioactivity. However, no significant breakthrough has been achieved in endowing PMMA bone cement with bioactivity while maintaining or improving its mechanical properties. In this study, bioactive PMMA&LDH composite bone cement has been successfully prepared by incorporating 15 wt% MgAl-LDH microsheets into PMMA. The addition of LDH reduced the peak heat of polymerization of PMMA and improved its mechanical properties as well. The synthesized PMMA&LDH bone cement possesses good biocompatibility. It can promote bone formation *in vivo* and improve the interfacial osseointegration between the bone and bone cement. Moreover, the key osteogenic pathways of human BMSCs activated by PMMA&LDH bone cement have also been revealed. Therefore, such a bioactive PMMA&LDH composite bone cement is expected to be a promising biomaterial for orthopedic surgeries.

METHODS

Materials. Polymethyl methacrylate bone cement (PMMA, Johnson & Johnson, USA) and mineralized collagen I (MCOL-I, Allgens Medical, China) were obtained from commercial sources without further purification, and MCOL-I is referred to as COL-I in the following. Total RNA

extraction kit was purchased from Gibco (Thermo Fisher Scientific, USA). Human bone marrow-derived mesenchymal stem cells (hBMSCs) were acquired from ScienCell (Catalog #7500, USA), and the medium is mesenchymal stem cell medium (MSCM, Catalog #7501, ScienCell, USA). Human mesenchymal stem cell osteogenic differentiation medium was purchased from Cyagen (Catalog #HUXMA-90021). The CCK-8 reagent was obtained from Dojindo (Kumamoto, Japan). Anti-RUNX2 antibody (#ab23981), anti-ALP antibody (#ab229126), anti-P-p38 antibody (#ab38238), anti-p38 antibody (#ab170099), and anti-GAPDH antibody (#ab9485) from rabbit were purchased from Abcam (Massachusetts, US). Anti-rabbit IgG/HRP antibody from goat (074-15-06) was purchased from Kirkegaard & Perry Laboratories, Inc. (Gaithersburg, USA). Alizarin Red S and Alkaline Phosphatase Staining Solution were acquired from Sigma (San Francisco, USA).

Synthesis of MgAl-LDH Microsheets and Modified PMMA Bone Cement. Typically, $Mg(NO_3)_2 \cdot 6H_2O$ (2 mmol), $Al(NO_3)_3 \cdot 9H_2O$ (1 mmol) and urea (12 mmol) were dissolved in 70 mL deionized water. The mixture was transferred to a 100 mL teflon-lined stainless steel autoclave and heated at 100 °C for 24 h. The resultant MgAl-LDH was washed with distilled water and then dried in air at 60 °C. Commercially available PMMA was obtained from Johnson & Johnson®, USA. The total weight of the tested MMA (100 wt%), MMA&COL-I (85 wt% & 15 wt%), MMA&LDH (85 wt% & 15 wt%), and MMA&COL-I&LDH (70 wt% & 15 wt% & 15 wt%) is 10 g. For experiments, PMMA was prepared according to the manufacturer's instructions. Briefly, the liquid MMA monomer was added to the powder of pre-polymerized PMMA and COL-I and/or LDH to initiate the polymerization reaction of MMA at room temperature (25 °C) for 20 min after the powder was mixed thoroughly, and the corresponding molds were filled to obtain specific-shape materials.

Temperature of Polymerization Reaction and Setting Time Tests. The total weight of the

tested MMA (100 wt%), MMA&COL-I (85 wt%&15 wt%), MMA&LDH (85 wt%&15 wt%), and MMA&COL-I&LDH (70 wt%&15 wt%&15 wt%) is 10 g. After the powder of pre-polymerized PMMA and COL-I and/or LDH was mixed thoroughly, the liquid MMA monomer was added to the powder to initiate the polymerization reaction of MMA (Scheme 1). 20 mL of syringe barrel was served as a reaction vessel for MMA polymerization. FLUKE infrared imager (FLUKE, Washington, USA) was used to detect the temperature changes of polymerization reaction. The setting time of PMMA was measured with a Vicat needle (LeiYun Experimental Apparatus Manufacturing Co., Ltd., Shanghai, China) according to ISO9597-1989E. The setting time was defined as the time that the heavy needle (306 g, Ø 1.140 mm) no longer left a visible print on the surface of the materials. Three replicates were conducted for each group and average values were calculated. The polymerization reaction and setting time tests were measured at 23 °C and the relative humidity was 50% (Figure S3a).

Mechanical Property Tests. A universal material testing machine (Instron-5880, Instron, Norwood, MA, USA) was used to test the mechanical properties of PMMA, and COL-I and/or LDH modified PMMA according to ISO 5833-2002 (annex E and F). Cylindrical specimens with a diameter of 6 mm and a height of 12 mm were fabricated using a stainless-steel mold for compressive strength and compressive modulus tests (Figure S4a-b). Flat plate specimens with a length of 75 mm, a width of 10 mm, and a thickness of 3.3 mm were prepared on polytetrafluoroethylene (PTFE) mold, and the four-point bending strength and bending modulus were tested (Figure S4c-d).

The bending strength, compressive strength and bending modulus for each specimen were calculated according to the expressions in accordance with ISO 5833-2002. Moreover, the

compressive modulus of each specimen were calculated according to the slope of the linear region of the stress-strain curve, which is derived from the displacement-load curve recorded by the testing machine, and the height and diameter of the specimen.

Preparation of Extracts and Detection of Magnesium Ions Concentrations. Three samples (2.5 mm thickness, 6.0 mm diameter) of PMMA&LDH and PMMA&COL-I&LDH bone cements for each group were immersed in 2.5 mL osteogenic differentiation medium. The osteogenic differentiation medium was totally replaced with fresh medium after each 48 h. The magnesium ion concentrations released from PMMA&LDH and PMMA&COL-I&LDH bone cements were monitored at Day 1, 3, 5, 7, 9, 11, and 13 by inductively coupled plasma optical emission spectrometry (ICP- OES; Perkin Elmer, Optima 2100DV).

Cytocompatibility Evaluation *in vitro.* PMMA, PMMA&COL-I, PMMA&LDH, and PMMA&COL-I&LDH were made into disc-shaped specimens respectively with a diameter of 6 mm and a thickness of 2.5 mm after fully mixed with liquid initiator (Figure S3b). All specimens were sterilized with ethylene oxide before the cytotoxicity test. Initially, 10,000 cells were seeded in the lower chamber of a 24-well Trans well plate with 3 μm pore diameter (Corning, #3415, USA) for 12 hours to allow the cells to fully adhere to the wells, and then 1 disc-shaped specimen was added to the upper chamber. Besides, 1 disc-shaped specimen was fixed to the bottom of 24-well plate using collagen for 1 hour and 10,000 cells were directly seeded on the surface of disc-shaped specimen. Three parallel wells were set for each group. The plates were placed in an atmosphere of 37 °C, 5% CO2, and 95% relative humidity. The blank control group consisted of seeded cells only. CCK-8 assay was carried out on Day 1, 3, 5, and 7, and OD values at 450 ± 5 nm were measured by a multifunctional full-wavelength microplate reader (Varioskan Flash; Thermo Fisher Scientific, USA).

Moreover, flow cytometry assay was carried out on Day 3 by FACSCanto plus (BD Biosciences, USA).

Alkaline Phosphatase and Alizarin Red S Staining Assays. The process of specimen preparation and specimen sterilization were the same as that in the section of cytocompatibility evaluation. Osteogenic differentiation medium (ODM) and 6-well Trans well plate with 3 μm pore diameter (Corning, #3492, USA) were selected to culture cells indirectly. 30,000 cells were seeded into the lower chamber, and PMMA, PMMA&COL-I, PMMA&LDH, and PMMA&COL-I&LDH specimens were added to each upper chamber 12 hours later (3 specimens in each upper chamber). Besides, 3 specimens of each group were fixed to the bottom of 6-well plate and then 30,000 cells were directly seeded on the surface of specimens. On Day 14, the upper chamber and ODM were totally removed, and the cells in each well were washed twice with 2 mL of PBS. Afterwards, the cells were fixed with 2 mL of 4% paraformaldehyde (Gibco, USA) for 15 min. After washing 3 times with distilled water, each well was incubated with 2 mL of alizarin red S solution (Solarbio Life Science, Beijing, China) for 15 min or 2 mL of alkaline phosphatase staining solution (Solarbio Life Science, Beijing, China) for 20 min. Subsequently, all cells were washed 3 times with PBS and observed with an Eclipse80i microscope (Nikon, Minato, Japan).

Transcriptome Sequencing. The process of specimen preparation and specimen sterilization were the same as that in the section of cytocompatibility evaluation. After the cells were cultured with ODM together with tested materials in a 6-well Trans Well plate for 7 days (3 specimens in each upper chamber), the ODM supernatant was totally removed, and the cells were washed three times with 2 mL of PBS. Subsequently, 1 mL of TRIzol was used to lyse the cells in each well, and the TRIzol solution containing lytic cells was transferred to a 1.5 mL EP tube. After the RNA of the

samples was totally extracted using RNA extraction kit and the DNA was digested with DNase (Thermo Fisher, USA), the magnetic beads with Oligo (dT) were utilized to enrich the eukaryotic mRNA, and then the interrupting reagent was added to interrupt mRNA into short fragments. The interrupted mRNA served as a template in the following steps. Six-base random primers were used to synthesize one-strand cDNA, and then a two-strand reaction system was prepared to synthesize two-strand cDNA. Subsequently, the double-strand cDNA was purified and repaired. Finally, PCR amplification was performed after the fragment size was selected. After the constructed library is qualified evaluated by the Agilent 2100 Bioanalyzer, the Illumina sequencer was used for sequencing. The sequencing and library construction process is shown in Figure S11a, and the transcriptome sequencing analysis process is shown in Figure S11b. Moreover, the network and pathway analysis were conducted by Ingenuity Pathway Analysis software (IPA®, v01-04, QIANGEN Redwood City, CA, USA).

Quantitative Real-Time Polymerase Chain Reaction. The method of cell culture was the same as that in the section of transcriptome sequencing. On Day 7, the RNA extraction kit was used to extract total RNA from the cells and the detailed steps are as follows: cells were washed twice with 2 mL of PBS and then 1 mL of TRIzol reagent (Life Technologies Corporation, Carlsbad, USA) was added to each well. After lysing for 15 min, the TRIzol reagent containing lytic cells were transferred to a microtube and vigorously mixed with 200 μL of chloroform (Merck KGaA, Darmstadt, Germany). After centrifugation at 12,000 g for 15 min at 4 °C (Legend Micro 17R; Thermo Fisher Scientific), the supernatant was collected to perform the total RNA isolation (Ambion Inc., Austin, USA) according to the manufacturer's protocol. The concentration of extracted RNA was evaluated by a NanoDrop spectrophotometer (Thermo Fisher Scientific, USA). Then the

extracted RNA was subsequently transcribed into cDNA through a high capacity RNA-to-cDNA kit (Applied Biosystems, Foster City, USA). The transcriptional levels of *Alp*, *Runx2*, *p38*, and *P-p38* were compared among PMMA, PMMA&COL-I, PMMA&LDH, and PMMA&COL-I&LDH groups. *Gapdh* served as the reference gene. Specific sequences of primers were designed with Primer (version 5.0, Premier Biosoft International, USA) (Table S1). The relative gene expression was calculated with the ΔΔcT method.

Western Blot Assay. The method of cell culture was the same as that in the section of transcriptome sequencing. The total cell proteins were collected using RIPA Lysis and Extraction Buffer (Invitrogen, Carlsbad, CA, cat. no. 89901) on Day 7. PierceTM Rapid Gold BCA Protein Assay Kit (#53225, Invitrogen, Carlsbad, CA) was utilized to measure the protein concentration. Protein (approximately 30 μg) was loaded with SDS-PAGE gel and then transferred to a polyvinylidene difluoride (PVDF) membrane on ice. Subsequently, the PVDF membrane was blocked with 5% dilute skim milk in Tris Buffered Taline Tween (TBST) at room temperature for 45 min. After washing with enough TBST, the membrane and primary antibodies were incubated together overnight at 4 °C. After that, the membrane was washed three times with TBST, and then incubated with the secondary antibodies at room temperature for 45 min. The target bands were visualized by enhanced chemiluminescence (ECL, Thermo Fisher Scientific, CA, USA) technology and the optical density of the bands was analyzed by Bio-Rad image analysis software (Bio-Rad, Hercules, CA, USA). *Gapdh* was used as the reference gene. The primary antibodies used in the present study were anti-RUNX2 (1:1000, Abcam, #ab23981), anti-ALP (1:1000, Abcam, #ab229126), anti-p38 (1:1000, Abcam, #ab170099), anti-P-p38 (1:1000, Abcam, #ab38238), and anti-GAPDH (1:1000, Abcam, #ab9485).

Establishment of Rabbit Skull Bone Defect and Sequential Fluorescent Labeling Assays. The animal experiment was performed in line with the National Institutes of Health Guidelines for the use of experimental animals, and the protocol was approved by the Animal Care and Use Committee of Peking Union Medical College Hospital. A total of 15 bone mature and healthy New Zealand white rabbits with an average weight of 2.5 kg were purchased from Charles River Laboratories (Charles River, USA), and fed in a humidity (40-60%) and temperature (25 °C) controlled room with a 12 h light/dark cycle. After 1 week for acclimatization, the 15 rabbits were randomly divided into 3 groups, and then all rabbits were anaesthetized by injecting pentobarbital (3%, 1 mL/kg) into the ear vein. On the flat part of the skull, a trephine was utilized to make four full-thickness skull bone defects with a diameter of 6 mm (Figure S17a-c). Four biomaterials made of three modified PMMA and pure PMMA were placed in corresponding positions (Figure S17d, Figure 5b). Absorbable suture (Jinhuan Corp, Shanghai, China) was utilized to suture the subcutaneous tissue and skin in turn. Rabbits undergoing operation were injected intra-muscularly with 200,000 U of penicillin (Shengwang Corp, Shandong, China) three times immediately, 24 hours, and 48 hours after surgery. Moreover, two types of fluorochromes were injected intraperitoneally in a sequence of 30 mg/kg Alizarin Red S (Sigma, USA) and 20 mg/kg Calcein (Sigma, USA) immediately, and 1 month after surgery, respectively.

The evaluation of biological safety *in vivo.* The heart, liver, spleen, kidney, and spinal cord were harvested immediately, 1 month, and 2 months after surgery, and then soaked in neutral formalin (Solarbio Life Science, Beijing, China). Subsequently, tissues were sliced to 50 μm thickness by rotary microtome (RM2255; Leica, Germany) after embedding, gradient dehydration, and transparentizing. Histological structures were stained by hematoxylin-eosin (H&E) staining and

verified by Eclipse 80i microscope (Nikon, Japan).

Micro Computed Tomography and Hard Tissue Section. The rabbits were sacrificed by air embolism immediately, 1 month, and 2 months after surgery, and then all the skulls were harvested and soaked in neutral formalin. The skulls were scanned by micro-computed tomography (micro-CT; Siemens, Germany) to evaluate the degree of interface osseointegration between material and bone. The hard tissue section involves 10 steps. Step 1: the flat part of skull (namely skull specimens) containing four filled bone defects was cut off. Step 2: all skull specimens were fixed in formalin solution for 48 hours, and then rinsed in running water for 24 hours. Step 3: the skull specimens were dehydrated using 70%, 75%, 80%, 85%, 90%, and 95% alcohol for 24 hours respectively. Step 4: the skull specimens were put in absolute alcohol and Technovit 7200 resin solution (volume ratio 3:7) for 2 days. Step 5: the skull specimens were put in absolute alcohol and Technovit 7200 resin solution (volume ratio 1:1) for 2 days. Step 6: all skull specimens were soaked in Technovit 7200 resin solution I and Technovit 7200 resin solution II for 7 days and 3 days, respectively. Step 7: light curing machine was utilized to embed hard tissues. Step 8: German EXAKT300CP hard tissue microtome was used to cut the skull specimens into 200 μm slices. Step 9: slices with a thickness of 200 μm were progressively ground to 25 μm by 320, 800, and 1200 mesh in turn. Step 10: slices with a thickness of 25 μm were polished with 4000 mash sandpaper.

Laser Scanning Confocal Microscopy Scanning and Acid Fuchsin Stain. After hard tissue section, the slices with a thickness 25 μm were scanned by laser scanning confocal microscopy (LSCM, Leica, Germany) to show the degree of newly formed bone growing into PMMA and modified PMMA, and then the scanned images were automatically stitched into complete images. The regenerated bone was quantitatively analyzed in acid fuchsin stain sections using Image J 1.52a

1.52v software. Methylene blue acid fuchsin staining was employed to reveal the newly formed bone which was quantitatively analyzed using Image J 1.52a 1.52v software.

Statistical Analysis. The Kolmogorov–Smirnov test was utilized to estimate the distribution of data. The continuous variables of normal distribution were expressed as the mean ± standard deviation. One-way analysis of variance (ANOVA) was used for statistical analysis, followed by the Student–Newman–Keuls post hoc test.

ASSOCIATED CONTENT

Supporting Information

The Supporting Information is available free of charge *via* the Internet at http://pubs.acs.org.

The primer sequences of *Runx2, Alp, p38, P-p38 and Gapdh* (Table S1); Atomic force microscope and energy dispersive spectrometer mappings of PMMA and modified PMMA (Figure S1-S2); Preparation for polymerization reaction and setting time tests, and preparation of specimens for biological experiments (Figure 3); Preparation of specimens and mechanical property tests (Figure S4); Tissue structure of heart, liver, spleen, kidney and spinal cord treated with PMMA and modified PMMA (Figure S5-S9); Concentrations of magnesium ions released from PMMA&LDH and PMMA&COL-I&LDH (Figure S10); The flow chart of database construction and bioinformatics analysis of transcriptome sequencing (Fgure S11); ERK/MAPK, p38/MAPK, FGF and TGF-β signal pathway upregulated by PMMA&LDH (Figure S12-S16); The process of surgical operation and specimen implantation of animal experiment (Figure S17).

AUTHOR INFORMATION

Corresponding Authors

Xisheng Weng – *Department of Orthopedic Surgery, Peking Union Medical College Hospital, Peking Union Medical College & Chinese Academy of Medical Sciences, Beijing 100730, China*; orcid.org/0000-0003-0959-8988; Email: xshweng@pumch.cams.cn

Ruizheng Liang – *State Key Laboratory of Chemical Resource Engineering, Beijing Advanced Innovation Center for Soft Matter Science and Engineering, Beijing University of Chemical Technology, Beijing 100029, China*; orcid.org/0000-0002-3930-9625; Email: liangrz@mail.buct.edu.cn

Authors

Yingjie Wang – *Department of Orthopedic Surgery, Peking Union Medical College Hospital, Peking Union Medical College & Chinese Academy of Medical Sciences, Beijing 100730, China*

Songpo Shen – *Department of Orthopedic Surgery, Beijing Tongren Hospital, Capital Medical University, Beijing 100730, China; Department of Orthopedic Surgery, Peking Union Medical College Hospital, Peking Union Medical College & Chinese Academy of Medical Sciences, Beijing 100730, China*

Tingting Hu – *State Key Laboratory of Chemical Resource Engineering, Beijing Advanced Innovation Center for Soft Matter Science and Engineering, Beijing University of Chemical Technology, Beijing 100029, China*

Gareth R. Williams – *UCL School of Pharmacy, University College London, 29-39 Brunswick Square, London WC1N 1AX, UK*

Yanyan Bian – *Department of Orthopedic Surgery, Peking Union Medical College Hospital, Peking*

Union Medical College & Chinese Academy of Medical Sciences, Beijing 100730, China

Bin Feng – *Department of Orthopedic Surgery, Peking Union Medical College Hospital, Peking Union Medical College & Chinese Academy of Medical Sciences, Beijing 100730, China*

Author Contributions

[#] Y. W. and S. S. contributed equally to this work.

Notes

The authors declare no competing financial interest.

ACKNOWLEDGEMENTS

R. L. would like to thank the funding support from National Natural Science Foundation of China (No. 21971007, 21671013) and Fundamental Research Funds for the Central Universities (XK1802-6, XK1803-05, 12060093063). X. W. would like to thank the funding support from National Natural Science Foundation of China (No. 81630064, 81871786, 81272009, 81572143, 81611130091).

REFERENCES

1. Colas, S.; Collin, C.; Piriou, P.; Zureik, M. Association between Total Hip Replacement Characteristics and 3-Year Prosthetic Survivorship: A Population-Based Study. *JAMA Surg.* **2015**, *150*, 979–988.

2. Okike, K.; Chan, P. H.; Prentice, H. A.; Paxton, E. W.; Burri, R. A. Association between Uncemented *vs* Cemented Hemiarthroplasty and Revision Surgery among Patients with Hip Fracture. *JAMA* **2020**, *323*, 1077–1084.

3. Wang, L.; Zhu, L.; Wang, Z.; Lou, A.; Yang, Y.; Guo, Y.; Liu, S.; Zhang, C.; Zhang, Z.; Hu, H.; Yang, B.; Zhang, P.; Ou Yang, H.; Zhang, Z. Development of a Centrally Vascularized Tissue Engineering Bone Graft with the Unique Core-Shell Composite Structure for Large Femoral Bone Defect Treatment. *Biomaterials* **2018**, *175*, 44–60.

4. Xu, C.; Ma, B.; Peng, J.; Gao, L.; Xu, Y.; Huan, Z.; Chang, J. Tricalcium Silicate/Graphene Oxide Bone Cement with Photothermal Properties for Tumor Ablation. *J. Mater. Chem. B* **2019**, *7*, 2808–2818.

5. Vaishya, R.; Chauhan, M.; Vaish, A. Bone Cement. *J. Clin. Orthop. Trauma* **2013,** *4*, 157–163.

6. Sathish, S.; Ishizu, N.; Shen, A. Q. Air Plasma-Enhanced Covalent Functionalization of Poly(methyl Methacrylate): High-Throughput Protein Immobilization for Miniaturized Bioassays. *ACS Appl. Mater. Inter.* **2019**, *11*, 46350–46360.

7. Saruta, J.; Ozawa, R.; Hamajima, K.; Saita, M.; Sato, N.; Ishijima, M.; Kitajima, H.; Ogawa, T. Prolonged Post-Polymerization Biocompatibility of Polymethylmethacrylate-Tri-*N*-Butylborane (PMMA-TBB) Bone Cement. *Materials* **2021**, *14*, 1289.

8. Gundapaneni, D.; Goswami, T. Thermal Isotherms in PMMA and Cell Necrosis during Total Hip

Arthroplasty. *J. Appl. Biomater. Funct.* **2014**, *12*, 193–202.

9. Zhai, Q.; Han, F.; He, Z.; Shi, C.; Zhou, P.; Zhu, C.; Guo, Q.; Zhu, X.; Yang, H.; Li, B. The "Magnesium Sacrifice" Strategy Enables PMMA Bone Cement Partial Biodegradability and Osseointegration Potential. *Int. J. Mol. Sci.* **2018**, *19*, 1746.

10. Chen, L.; Tang, Y.; Zhao, K.; Zha, X.; Liu, J.; Bai, H.; Wu, Z. Fabrication of the Antibiotic-Releasing Gelatin/PMMA Bone Cement. *Colloid. Surface. B.* **2019**, *183*, 110448.

11. Goldring, S. R.; Clark, C. R.; Wright, T. M. The Problem in Total Joint Arthroplasty: Aseptic Loosening. *J. Bone Joint Surg. Am.* **1993**, *75*, 799–801.

12. Omar, M.; Klawonn, F.; Brand, S.; Stiesch, M.; Krettek, C.; Eberhard, J. Transcriptome-Wide High-Density Microarray Analysis Reveals Differential Gene Transcription in Periprosthetic Tissue from Hips with Chronic Periprosthetic Joint Infection *vs* Aseptic Loosening. *J. Arthroplasty* **2017**, *32*, 234–240.

13. Schunck, A.; Kronz, A.; Fischer, C.; Buchhorn, G. H. Release of Zirconia Nanoparticles at the Metal Stem-Bone Cement Interface in Implant Loosening of Total Hip Replacements. *Acta Biomater.* **2016**, *31*, 412–424.

14. Meinardi, J. E.; Valstar, E. R.; Van Der Voort, P.; Kaptein, B. L.; Fiocco, M.; Nelissen, R. G. H. H. Palacos Compared to Palamed Bone Cement in Total Hip Replacement: A Randomized Controlled Trial. *Acta Orthop.* **2016**, *87*, 473–478.

15. Ni, G. X.; Chiu, K. Y.; Lu, W. W.; Wang, Y.; Zhang, Y. G.; Hao, L. B.; Li, Z. Y.; Lam, W. M.; Lu, S. B.; Luk, K. D. K. Strontium-Containing Hydroxyapatite Bioactive Bone Cement in Revision Hip Arthroplasty. *Biomaterials* **2006**, *27*, 4348–4355.

16. Ni, G. X.; Lin, J. H.; Chiu, P. K. Y.; Li, Z. Y.; Lu, W. W. Effect of Strontium-Containing

Hydroxyapatite Bone Cement on Bone Remodeling Following Hip Replacement. *J. Mater. Sci-Mater. M.* **2010**, *21*, 377–384.

17. Ni, G. X.; Choy, Y. S.; Lu, W. W.; Ngan, A. H. W.; Chiu, K. Y.; Li, Z. Y.; Tang, B.; Luk, K. D. K. Nano-Mechanics of Bone and Bioactive Bone Cement Interfaces in a Load-Bearing Model. *Biomaterials* **2006**, *27*, 1963–1970.

18. Tan, H.; Guo, S.; Yang, S.; Xu, X.; Tang, T. Physical Characterization and Osteogenic Activity of the Quaternized Chitosan-Loaded PMMA Bone Cement. *Acta Biomater.* **2012**, *8*, 2166–2174.

19. Arora, M.; Chan, E. K.; Gupta, S.; Diwan, A. D. Polymethylmethacrylate Bone Cements and Additives: A Review of the Literature. *World J. Orthop.* **2013**, *4*, 67–74.

20. Boger, A.; Bohner, M.; Heini, P.; Verrier, S.; Schneider, E. Properties of an Injectable Low Modulus PMMA Bone Cement for Osteoporotic Bone. *J. Biomed. Mater. Res. B.* **2008**, *86*, 474–482.

21. Kim, S. B.; Kim, Y. J.; Yoon, T. L.; Park, S. A.; Cho, I. H.; Kim, E. J.; Kim, I. A.; Shin, J. W. The Characteristics of a Hydroxyapatite-Chitosan-PMMA Bone Cement. *Biomaterials* **2004**, *25*, 5715–5723.

22. Sukur, E.; Akar, A.; Topcu, H. N.; Cicekli, O.; Kochai, A.; Turker, M. The Effect of *N*-Acetylcysteine on Mechanical Fatigue Resistance of Antibiotic-Loaded Bone Cement. *J. Orthop. Surg. Res.* **2018**, *13*, 132.

23. Kapusetti, G.; Mishra, R. R.; Srivastava, S.; Misra, N.; Singh, V.; Roy, P.; Singh, S. K.; Chakraborty, C.; Malik, S.; Maiti, P. Layered Double Hydroxide Induced Advancement in Joint Prosthesis Using Bone Cement: The Effect of Metal Substitution. *J. Mater. Chem. B* **2013**, *1*, 2275–2288.

24. Gao, R.; Yan, D. Layered Host-Guest Long-Afterglow Ultrathin Nanosheets: High-Efficiency

Phosphorescence Energy Transfer at 2D Confined Interface. *Chem. Sci.* **2017**, *8,* 590–599.

25. Gao, R.; Yan, D.; Evans, D. G.; Duan, X. Layer-By-Layer Assembly of Long-Afterglow Self-Supporting Thin Films with Dual-Stimuli-Responsive Phosphorescence and Antiforgery Applications. *Nano Res.* **2017**, *10*, 3606–3617.

26. Arif, M.; Yasin, G.; Luo, L.; Ye, W.; Mushtaq, M. A.; Fang, X.; Xiang, X.; Ji, S.; Yan, D. Hierarchical Hollow Nanotubes of NiFeV-Layered Double Hydroxides@CoVP Heterostructures towards Efficient, pH-Universal Electrocatalytical Nitrogen Reduction Reaction to Ammonia. *Appl. Catal. B-Environ.* **2020**, *265*, 118559

27. Chen, Y.; Zhu, R.; Ke, Q.; Gao, Y.; Zhang, C.; Guo, Y. MgAl Layered Double Hydroxide/Chitosan Porous Scaffolds Loaded with PFTα to Promote Bone Regeneration. *Nanoscale* **2017**, *9*, 6765–6776.

28. Wang, Y.; Mei, X.; Bian, Y.; Hu, T.; Weng, X.; Liang, R.; Wei, M. Magnesium-Based Layered Double Hydroxide Nanosheets: A New Bone Repair Material with Unprecedented Osteogenic Differentiation Performance. *Nanoscale* **2020**, *12*, 19075–19082.

29. Yu, Z.; Hu, P.; Xu, Y.; Bao, Q.; Ni, D.; Wei, C.; Shi, J. Efficient Gene Therapy of Pancreatic Cancer *via* a Peptide Nucleic Acid (PNA)-Loaded Layered Double Hydroxides (LDH) Nanoplatform. *Small* **2020**, *16*, 1907233.

30. Wang, D.; Ge, N.; Yang, T.; Peng, F.; Qiao, Y.; Li, Q.; Liu, X. NIR-Triggered Crystal Phase Transformation of NiTi-Layered Double Hydroxides Films for Localized Chemothermal Tumor Therapy. *Adv. Sci.* **2018**, *5*, 1700782.

31. Zhang, Y.; Zheng, J.; Yue, Y.; Zhao, H.; Li, F.; Guo, L. Bioinspired LDH-Based Hierarchical Structural Hybrid Materials with Adjustable Mechanical Performance. *Adv. Funct. Mater.* **2018**, *28*,

1801614.

32. Dalmas, F.; Pearson, S.; Gary, B.; Chenal, J. M.; Bourgeat Lami, E.; Prevot, V.; Chazeau, L. Tailored Microstructure and Mechanical Properties of Nanocomposite Films Made from Polyacrylic/LDH Hybrid Latexes Synthesized by RAFT-Mediated Emulsion Polymerization. *Polym. Chem-UK.* **2018**, *9*, 2590–2600.

33. Luo, X.; Shen, J.; Ma, Y.; Liu, L.; Meng, R.; Yao, J. Robust, Sustainable Cellulose Composite Aerogels with Outstanding Flame Retardancy and Thermal Insulation. *Carbohyd. Polym.* **2020**, *230,* 115623.

34. Wang, X.; Kalali, E. N.; Wang, D. Renewable Cardanol-Based Surfactant Modified Layered Double Hydroxide as a Flame Retardant for Epoxy Resin. *ACS Sustain. Chem. Eng.* **2015**, *3*, 3281–3290.

35. Yue, X.; Zhang, T.; Yang, D.; Qiu, F.; Wei, G.; Zhou, H. Multifunctional Janus Fibrous Hybrid Membranes with Sandwich Structure for On-Demand Personal Thermal Management. *Nano Energy* **2019**, *63,* 103808.

36. Jiang, N.; Guo, Z.; Sun, D.; Li, Y.; Yang, Y.; Chen, C.; Zhang, L.; Zhu, S. Promoting Osseointegration of Ti Implants through Micro/Nanoscaled Hierarchical Ti Phosphate/Ti Oxide Hybrid Coating. *ACS Nano* **2018**, *12*, 7883-7891.

37. Boyan, B. D.; Lotz, E. M.; Schwartz, Z. (*) Roughness and Hydrophilicity as Osteogenic Biomimetic Surface Properties. *Tissue Eng. Pt. A* **2017**, *23*, 1479–1489.

38. Kurata, K.; Matsushita, J.; Furuno, A.; Fujino, J.; Takamatsu, H. Assessment of Thermal Damage in Total Knee Arthroplasty Using an Osteocyte Injury Model. *J. Orthop. Res.* **2017**, *35*, 2799–2807.

39. Fukushima, H.; Hashimoto, Y.; Yoshiya, S.; Kurosaka, M.; Matsuda, M.; Kawamura, S.; Iwatsubo, T. Conduction Analysis of Cement Interface Temperature in Total Knee Arthroplasty. *Kobe J. Med. Sci.* **2002**, *48*, 63–72.

40. Boger, A.; Wheeler, K.; Montali, A.; Gruskin, E. NMP-Modified PMMA Bone Cement with Adapted Mechanical and Hardening Properties for the Use in Cancellous Bone Augmentation. *J. Biomed. Mater. Res. B.* **2009**, *90*, 760–766.

41. López, A.; Mestres, G.; Ott, M. K.; Engqvist, H.; Ferguson, S. J.; Persson, C.; Helgason, B. Compressive Mechanical Properties and Cytocompatibility of Bone-Compliant, Linoleic Acid-Modified Bone Cement in a Bovine Model. *J. Mech. Behav. Biomed.* **2014**, *32*, 245–256.

42. Robo, C.; Hulsart Billström, G.; Nilsson, M.; Persson, C. *In Vivo* Response to a Low-Modulus PMMA Bone Cement in an Ovine Model. *Acta Biomater.* **2018**, *72*, 362–370.

43. Liu, W.; Ou Yang, W.; Zhang, C.; Wang, Q.; Pan, X.; Huang, P.; Zhang, C.; Li, Y.; Kong, D.; Wang, W. Synthetic Polymeric Antibacterial Hydrogel for Methicillin-Resistant Staphylococcus Aureus-Infected Wound Healing: Nanoantimicrobial Self-Assembly, Drug- and Cytokine-Free Strategy. *ACS Nano* **2020**, *14*, 12905–12917.

44. Las, D. E.; Verwilghen, D.; Mommaerts, M. Y. A Systematic Review of Cranioplasty Material Toxicity in Human Subjects. *J. Craniomaxillofac. Surg.* **2021**, *49*, 34–46.

45. Luu, A.; Syed, F.; Raman, G.; Bhalla, A.; Muldoon, E.; Hadley, S.; Smith, E.; Rao, M. Two-Stage Arthroplasty for Prosthetic Joint Infection: A Systematic Review of Acute Kidney Injury, Systemic Toxicity and Infection Control. *J. Arthroplasty* **2013**, *28*, 1490–1498.

46. Van Vugt, T. A. G.; Arts, J. J.; Geurts, J. A. P. Antibiotic-Loaded Polymethylmethacrylate Beads and Spacers in Treatment of Orthopedic Infections and the Role of Biofilm Formation. *Front.*

Microbiol. **2019**, *10*, 1626.

47. Xue, Y.; Niu, W.; Wang, M.; Chen, M.; Guo, Y.; Lei, B. Engineering a Biodegradable Multifunctional Antibacterial Bioactive Nanosystem for Enhancing Tumor Photothermo-Chemotherapy and Bone Regeneration. *ACS Nano* **2020**, *14*, 442–453.

48. Zhou, K.; Yu, P.; Shi, X.; Ling, T.; Zeng, W.; Chen, A.; Yang, W.; Zhou, Z. Hierarchically Porous Hydroxyapatite Hybrid Scaffold Incorporated with Reduced Graphene Oxide for Rapid Bone Ingrowth and Repair. *ACS Nano* **2019**, *13*, 9595–9606.

49. Lin, Z.; Wu, J.; Qiao, W.; Zhao, Y.; Wong, K. H. M.; Chu, P. K.; Bian, L.; Wu, S.; Zheng, Y.; Cheung, K. M. C.; Leung, F.; Yeung, K. W. K. Precisely Controlled Delivery of Magnesium Ions thru Sponge-Like Monodisperse PLGA/Nano-MgO-Alginate Core-Shell Microsphere Device to Enable *in Situ* Bone Regeneration. *Biomaterials* **2018**, *174*, 1–16.

50. Monfoulet, L. E.; Becquart, P.; Marchat, D.; Vandamme, K.; Bourguignon, M.; Pacard, E.; Viateau, V.; Petite, H.; Logeart Avramoglou, D. The pH in the Microenvironment of Human Mesenchymal Stem Cells Is a Critical Factor for Optimal Osteogenesis in Tissue-Engineered Constructs. *Tissue Eng. Pt. A* **2014**, *20*, 1827–1840.

51. Zhang, J.; Wang, X.; Suo, X.; Liu, X.; Liu, B.; Yuan, M.; Wang, G.; Liang, C.; Shi, H. Cellular Response of Escherichia coli to Photocatalysis: Flagellar Assembly Variation and Beyond. *ACS Nano* **2019**, *13*, 2004–2014.

52. He, J.; Sun, C.; Gu, Z.; Yang, Y.; Gu, M.; Xue, C.; Xie, Z.; Ren, H.; Wang, Y.; Liu, Y.; Liu, M.; Ding, F.; Leong, K. W.; Gu, X. Morphology, Migration, and Transcriptome Analysis of Schwann Cell Culture on Butterfly Wings with Different Surface Architectures. *ACS Nano* **2018**, *12*, 9660–9668.

53. Feliu, N.; Kohonen, P.; Ji, J.; Zhang, Y.; Karlsson, H. L.; Palmberg, L.; Nyström, A.; Fadeel, B. Next-Generation Sequencing Reveals Low-Dose Effects of Cationic Dendrimers in Primary Human Bronchial Epithelial Cells. *ACS Nano* **2015**, *9*, 146–163.

54. Song, Y.; Wu, H.; Gao, Y.; Li, J.; Lin, K.; Liu, B.; Lei, X.; Cheng, P.; Zhang, S.; Wang, Y.; Sun, J.; Bi, L.; Pei, G. Zinc Silicate/Nano-Hydroxyapatite/Collagen Scaffolds Promote Angiogenesis and Bone Regeneration *via* the p38 MAPK Pathway in Activated Monocytes. *ACS Appl. Mater. Inter.* **2020**, *12*, 16058–16075.

55. Gao, X.; Xue, Y.; Zhu, Z.; Chen, J.; Liu, Y.; Cheng, X.; Zhang, X.; Wang, J.; Pei, X.; Wan, Q. Nanoscale Zeolitic Imidazolate Framework-8 Activator of Canonical MAPK Signaling for Bone Repair. *ACS Appl. Mater. Inter.* **2021**, *13*, 97–111.

56. Zhu, Y.; Yang, Q.; Yang, M.; Zhan, X.; Lan, F.; He, J.; Gu, Z.; Wu, Y. Protein Corona of Magnetic Hydroxyapatite Scaffold Improves Cell Proliferation *via* Activation of Mitogen-Activated Protein Kinase Signaling Pathway. *ACS Nano* **2017**, *11*, 3690–3704.

57. Kim, J. M.; Shin, H. I.; Cha, S. S.; Lee, C. S.; Hong, B. S.; Lim, S.; Jang, H. J.; Kim, J.; Yang, Y. R.; Kim, Y. H.; Yun, S.; Rijal, G.; Lee Kwon, W.; Seo, J. K.; Gho, Y. S.; Ryu, S. H.; Hur, E. M.; Suh, P. G. DJ-1 Promotes Angiogenesis and Osteogenesis by Activating FGF Receptor-1 Signaling. *Nat. Commun.* **2012**, *3*, 1296.

58. Liu, W.; Wei, Y.; Zhang, X.; Xu, M.; Yang, X.; Deng, X. Lower Extent but Similar Rhythm of Osteogenic Behavior in hBMSCs Cultured on Nanofibrous Scaffolds *versus* Induced with Osteogenic Supplement. *ACS Nano* **2013**, *7*, 6928–6938.

59. Zhang, M.; Shi, J.; Xie, M.; Wen, J.; Niibe, K.; Zhang, X.; Luo, J.; Yan, R.; Zhang, Z.; Egusa, H.; Jiang, X. Recapitulation of Cartilage/Bone Formation Using IPSCs *via* Biomimetic 3D Rotary

Culture Approach for Developmental Engineering. *Biomaterials* **2020**, *260*, 120334.

60. Khorsand, B.; Acri, T. M.; Do, A. V.; Femino, J. E.; Petersen, E.; Fredericks, D. C.; Salem, A. K. A Multi-Functional Implant Induces Bone Formation in a Diabetic Model. *Adv. Healthc. Mater.* **2020**, *9* , 2000770.

61. Wu, M.; Chen, G.; Li, Y. TGF-β and BMP Signaling in Osteoblast, Skeletal Development, and Bone Formation, Homeostasis and Disease. *Bone Res.* **2016**, *4*, 16009.

62. Hankenson, K. D.; Gagne, K.; Shaughnessy, M. Extracellular Signaling Molecules to Promote Fracture Healing and Bone Regeneration. *Adv. Drug. Deliver. Rev.* **2015**, *94*, 3–12.

63. Sorkin, M.; Huber, A. K.; Hwang, C.; Carson IV, W. F.; Menon, R.; Li, J.; Vasquez, K.; Pagani, C.; Patel, N.; Li, S.; Visser, N. D.; Niknafs, Y.; Loder, S.; Scola, M.; Nycz, D.; Gallagher, K.; McCauley, L. K.; Xu, J.; James, A. W.; Agarwal, S.; Kunkel, S.; Mishina, Y.; Levi, B. Regulation of Heterotopic Ossification by Monocytes in a Mouse Model of Aberrant Wound Healing. *Nat. Commun.* **2020**, *11*, 722.

64. Li, J.; Ayoub, A.; Xiu, Y.; Yin, X.; Sanders, J. O.; Mesfin, A.; Xing, L.; Yao, Z.; Boyce, B. F. TGFβ-Induced Degradation of TRAF3 in Mesenchymal Progenitor Cells Causes Age-Related Osteoporosis. *Nat. Commun.* **2019**, *10*, 2795.

65. De Maeyer, R. P. H.; Van De Merwe, R. C.; Louie, R.; Bracken, O. V.; Devine, O. P.; Goldstein, D. R.; Uddin, M.; Akbar, A. N.; Gilroy, D. W. Blocking Elevated p38 MAPK Restores Efferocytosis and Inflammatory Resolution in the Elderly. *Nat. Immunol.* **2020**, *21*, 615–625.

66. Lin, K. C.; Moroishi, T.; Meng, Z.; Jeong, H. S.; Plouffe, S. W.; Sekido, Y.; Han, J.; Park, H. W.; Guan, K. L. Regulation of Hippo Pathway Transcription Factor TEAD by p38 MAPK-Induced Cytoplasmic Translocation. *Nat. Cell Biol.* **2017**, *19*, 996–1002.

67. Yuan, Z.; Tao, B.; He, Y.; Liu, J.; Lin, C.; Shen, X.; Ding, Y.; Yu, Y.; Mu, C.; Liu, P.; Cai, K. Biocompatible MoS(2)/PDA-RGD Coating on Titanium Implant with Antibacterial Property *via* Intrinsic ROS-Independent Oxidative Stress and NIR Irradiation. *Biomaterials* **2019**, *217*, 119290.

68. Laurenti, M.; Al Subaie, A.; Abdallah, M. N.; Cortes, A. R. G.; Ackerman, J. L.; Vali, H.; Basu, K.; Zhang, Y.; Murshed, M.; Strandman, S.; Zhu, J.; Makhoul, N.; Barralet, J. E.; Tamimi, F. Two-Dimensional Magnesium Phosphate Nanosheets Form Highly Thixotropic Gels That Up-Regulate Bone Formation. *Nano Lett.* **2016**, *16*, 4779–4787.

69. Tan, J.; Zhang, M.; Hai, Z.; Wu, C.; Lin, J.; Kuang, W.; Tang, H.; Huang, Y.; Chen, X.; Liang, G. Sustained Release of Two Bioactive Factors from Supramolecular Hydrogel Promotes Periodontal Bone Regeneration. *ACS Nano* **2019**, *13*, 5616–5622.